Molecular-Dynamics Study of the Crystal Structure of Iron Under the Earth's Inner Core Conditions

Hua Yang[1], Lei Wan[1], Yunguo Li[1,2*], Lidunka Vočadlo[3], John Brodholt[3,4]

[1]*State Key Laboratory of Lithospheric and Environmental Coevolution, School of Earth and Space Sciences, University of Science and Technology of China, Hefei 230026, China*
[2]*Deep Space Exploration Laboratory, Hefei 230026, China*
[3]*Department of Earth Sciences, University College London, Gower Street, London WC1E 6BT, United Kingdom*
[4]*Centre for Planetary Habitability, University of Oslo, Oslo, Norway*

*Corresponding author: Yunguo Li (liyunguo@ustc.edu.cn)

Abstract: The crystal structure of Earth's solid inner core is fundamental to understanding the chemical composition and dynamical evolution of the core. However, despite extensive research, the structure still remains controversial with competing hypotheses regarding the stability of various Fe phases (e.g., bcc, fcc, and hcp). In this paper, we review the studies on the crystal structure of Fe under inner core conditions, and find, in line with previous work, that the main challenges come from the small energy differences between these structures. This has led to a variety of different conclusions across varying theoretical methods and precision, including *ab initio*, force field and machine learning methods. To address this problem, we employ a Bain path thermodynamic integration approach to reach consistent conclusions among different methods; we find that bcc Fe is mechanically stable but thermodynamically less stable under inner core conditions. Using the energetics from the Bain path method as a benchmark, we establish the requirements for converging free energy calculations through a two-phase thermodynamic modelling approach. These calculations confirm that the hcp phase is the most stable, exhibiting the highest melting temperature regardless of the method used. This unified conclusion on the hcp phase as the stable crystal structure provides a robust foundation for future studies on Earth's core.

Plain Language Summary: Understanding the crystal structure of Earth's solid inner core is crucial for interpreting its chemical composition and dynamical evolution. Despite extensive efforts, the phase stability of iron (e.g., bcc, fcc, hcp) under core conditions remains heavily debated. The extreme *P-T* conditions of the inner core present a significant challenge to experiments, while the difficulty in theoretical studies stems from the minute energy differences among these structures. In this study, we introduce a thermodynamic-integration framework based on the Bain path, which offers enhanced accuracy and serves as a rigorous benchmark for evaluating phase-stability predictions. Applying this approach with stringent convergence criteria, we demonstrate that all commonly used potentials and computational methods uniformly confirm bcc as a metastable phase while hcp as the most stable phase under core conditions. Our findings reconcile previous disparities and establish a solid thermodynamic foundation for future studies of inner-core properties and dynamics.

Key Points:

1. Bcc Fe is mechanically stable under inner core conditions from either *ab initio* or force field methods
2. The thermodynamic metastability of bcc Fe is independent of the simulation cell size
3. Hcp Fe has the highest melting temperature thus being the most stable phase in the Earth's inner core

1. Introduction

The Earth's core, located ~2890 km beneath the surface with a radius of ~3480 km, comprises a solid inner core crystallising out from a liquid outer core (Dziewonski & Anderson, 1981). Understanding the composition and structure of the core is essential for comprehending various aspects of Earth's long-term evolution (e.g., Hirose et al., 2021). The crystal structure of the solid inner core is particularly important for determining the partitioning and abundance of light elements between the inner and outer core, as well as the core's temperature profile because of the different chemical potentials, densities and melting temperatures of various iron crystal structures. Previous studies suggest that the solid inner core is primarily composed of an Fe-rich solid solution, which may include substitutional and/or interstitial solid solutions of Fe with alloying elements such as Ni, Si, S, C, and H (Hikosaka et al., 2022; Li et al., 2018; Litasov & Shatskiy, 2016). Fe compounds like Fe_7C_3 and Fe_2S are unlikely to be significant constituents of the inner core as the eutectic points contain high concentrations of light elements and exhibit densities much lower than that of the inner core (Li et al., 2016; Tateno et al., 2019). Although it is well established that the inner core is primarily composed of Fe solid solution, the crystalline structure of the inner core remains debated.

The changes in the crystal structure of Fe at varying pressure and temperature (*P-T*) conditions are a critical scientific issue of interest in high-pressure physics and planetary sciences. At ambient *P-T* conditions, Fe exhibits a body-centred cubic (bcc) structure (α phase, which is not the close-packed with a space utilization rate of 68%); as temperature increases (~1185 K), it transforms into a face-centred cubic (fcc) structure (γ phase, stacking mode of ABCABC, close-packed with the highest space utilization rate of 74%), and at higher temperatures (~1666−1901 K), it reverts to a paramagnetic bcc structure (δ phase); while when the pressure exceeds ~15 GPa, it transitions to a hexagonal close-packed (hcp) structure (ε phase, stacking mode of ABAB with the highest space utilization rate of 74%) (Dewaele et al., 2006; Kraus et al., 2022; Mikhaylushkin et al., 2007; Pushcharovsky, 2019; Shen et al., 1998). Despite considerable efforts which have been made to investigate the phase diagram of Fe and its alloys under high *P-T* conditions, the precise crystalline structure of the inner core still remains controversial (Anzellini et al., 2013; Belonoshko et al., 2003; 2017; Dubrovinsky et al., 2007; Matsui &

Anderson, 1997; Ross et al., 1990; Stixrude, 2012; Sun et al., 2024; Tateno et al., 2010; Vočadlo et al., 2003). This has led to discrepancies in the inferred physical and chemical properties of the core, including estimates of core temperature (Alfè, 2009; Belonoshko et al., 2021; Boehler, 1993; Li et al., 2020; Sun et al., 2023; Williams et al., 1987), elastic properties (Ikuta et al., 2022; Li et al., 2018; Martorell et al., 2015), seismic anisotropy (Belonoshko, Simak et al., 2022; Sha & Cohen, 2010; Steinle-Neumann et al., 2001; Vočadlo, Wood, Alfè & Price, 2008), transport properties (Belonoshko et al., 2019; Gleason & Mao, 2013; Li & Scandolo, 2022; Xu et al., 2025), and thermal evolution of nucleation processes (Davies et al., 2019; Sun et al., 2022; Wilson et al., 2023).

The reason for the continual uncertainty in the correct phase of Fe at inner-core (IC) conditions is that accurately determining the crystal structure of Fe at the extreme *P-T* conditions of the Earth's core is a significant challenge. Early experiments conducted at room temperature by Brown & McQueen (1986) measured the elasticities of Fe under core pressures using shock wave techniques. They revealed discontinuous changes in Fe sound velocities, indicating a possible transition from hcp to fcc structure in the inner core. Subsequent experiments employing laser-heated diamond anvil cell (LHDAC) techniques not only suggested the potential presence of a stable bcc structure in the core (Dubrovinsky et al., 2007; Matsui & Anderson, 1997; Ross et al., 1990), but also demonstrated that the fcc structure could be stable within the *P-T* range of the inner core, exhibiting stability comparable to that of the hcp structure (Mikhaylushkin et al., 2007). Collectively, these previous findings suggested that the actual structure of the core may involve a complex phase with significant stacking faults. Advances in experimental techniques allowed later studies using LHDAC and laser-driven shock waves combined with X-ray diffraction to achieve *in situ* measurements of Fe crystal structures under high *P-T* conditions (Anzellini et al., 2013; Hrubiak et al., 2018; Kraus et al., 2022; Kuwayama et al., 2008; Sinmyo et al., 2019; Tateno et al., 2010; Turneaure et al., 2020; Zhang et al., 2023). However, discrepancies remain regarding the stability of hcp and bcc structures in these experiments. For instance, Hrubiak et al. (2018) reported the stabilisation of bcc, while Tateno et al. (2010) and other groups predominantly observed hcp (Anzellini et al., 2013; Kraus et al., 2022; Kuwayama et al., 2008; Sinmyo et al., 2019; Turneaure et al., 2020;

Zhang et al., 2023). These uncertainties are largely due to the challenges of experiments in simultaneously achieving the extreme *P-T* conditions (~330–360 GPa, ~5000–7000 K) of the inner core (Anderson, 2003), making it very difficult to reach a consensus among these experimental results to date.

From a theoretical perspective, a major challenge in precisely determining the crystal structure of the Earth's inner core lies in the closely competitive energies—on the order of tens of meV/atom between the various possible Fe phases, including bcc, fcc, and hcp structures (Belonoshko et al., 2011, 2021; Sun et al., 2023; Vočadlo et al., 2003; Vočadlo, Wood, Alfè, & Price, 2008). This energy competition leads to inconsistent conclusions across different methodologies, force fields, system sizes, and levels of computational precision (Belonoshko et al., 2017; Cui et al., 2013; Li & Scandolo, 2024a; Schultz et al., 2018; Stixrude & Cohen, 1995; Vočadlo et al., 2000). For instance, discrepancies arise between *ab initio* calculations using small cells and empirical potential simulations employing much larger cells (Belonoshko et al., 2017; Vočadlo et al., 2003). Variations in methodologies, as well as in the precision of vibrational entropy and free energy calculations, can result in contradictory conclusions (Belonoshko et al., 2021; Li & Scandolo, 2024a; Sun et al., 2023), even when identical system sizes and the same methods (EAM) are used (Belonoshko et al., 2017; Schultz et al., 2018). Consequently, these theoretical inconsistencies significantly impede a clear and unified understanding of both the crystalline structure and the associated properties of the Earth's inner core.

Indeed, a central theoretical debate on the crystal structure of Fe in the inner core is the stability of the bcc phase, particularly with respect to its mechanical and thermodynamic stabilities, while its dynamic stability at high temperatures has been firmly established (Côté et al., 2010; Luo et al., 2010; Vočadlo et al., 2003). According to density functional theory (DFT) calculations with small simulation cells, the bcc structure of Fe is generally believed to be unstable at IC conditions, mainly because it exhibits mechanical instability when subjected to tetragonal strain at high pressures (Soderlind et al., 1996; Stixrude & Cohen, 1995; Vočadlo, Wood, Gillan, et al., 2008). Even consideration of extremely high temperatures and the incorporation of appropriate amounts of light elements, such as Si and S, cannot overcome this

instability (Cui et al., 2013). However, this hypothesis has been recently challenged by studies proposing that the mechanical stability of the bcc structure may be enhanced by self-diffusion (Fe atoms diffusing like liquid, yet preserving all the properties of a solid), as demonstrated by the Born stability criteria through 2000-atom *ab initio* calculations (Belonoshko, Simak, et al., 2022) and 1000-atom deep-learning potential simulations (Li & Scandolo, 2024a). Further clarification is needed to obtain a clearer understanding of the mechanical stability of bcc Fe at IC conditions.

However, it is also the case that it has long been considered that the bcc phase is thermodynamically less stable with respect to the hcp and fcc structures, as evidenced by thermodynamic integration (TI) free energy calculations using various force fields, cell sizes, and reference systems (González-Cataldo & Militzer, 2023; Li & Scandolo, 2024b; Sun et al., 2023; Vočadlo et al., 2003; 2008). An alternative perspective has been put forward by Belonoshko et al. (2017), who proposed that the bcc structure may exhibit stability under specific conditions involving a large number of atoms ($N \geq 1024$) and extremely high temperatures (~7000 K). This thermodynamic stability was linked to a cooperative diffusion (collective drifting of Fe atoms) occurring in the <110> direction within an ultra-large system only, accompanied by a substantial increase in vibrational entropy (derived from the power spectrum of the velocity autocorrelation function), which is attributed to size-dependent diffusion effects. However, efforts to replicate this thermodynamic stability (calculated by TI) and the associated size effects using identical force fields, system sizes, and temperature-pressure conditions have proven unsuccessful (Schultz et al., 2018). Moreover, recent *ab initio* simulations (Ghosh et al., 2023) and deep-learning potential calculations (Li & Scandolo, 2024a) have demonstrated that cooperative diffusion behavior in the bcc structure can manifest even within a relatively small unit cell containing as few as 128 atoms. Nonetheless, their findings regarding the thermodynamic stability of the bcc phase and the direction of diffusion are inconsistent (Belonoshko et al., 2017; Ghosh et al., 2023; Li & Scandolo, 2024a). This discrepancy implies that the self-diffusion behavior of bcc Fe is not strongly dependent on the simulation size, whereas the accuracy and convergence of free energy calculations may be significantly influenced by the system size (Belonoshko et al., 2011; 2017), which, in turn, may

affect the thermodynamic results.

In light of these theoretical challenges and discrepancies, a more precise approach to free energy calculations and a comprehensive understanding of size effects is crucial for resolving the long-standing controversy regarding the stability of competing Fe phases under IC conditions. Generally, all theoretical results should be reproducible; however, thermodynamic calculations, particularly those involving entropy, impose stringent requirements on both simulation cell sizes and durations. Consequently, earlier studies may harbor inherent uncertainties, leading to conflicting conclusions. To address this, we propose using the Bain Path Thermodynamic Integration (BP-TI) technique (Ozolins, 2009; Vočadlo, Wood, Gillan, et al., 2008), which simultaneously evaluates the mechanical and thermodynamic stabilities of the bcc and fcc phases by integrating the differences in internal stress. The BP-TI does not work for bcc-hcp and fcc-hcp since there is no reversible path for these transitions. The BP-TI method eliminates the need for an additional reference system and avoids direct entropy calculations to determine thermodynamic properties. Instead, it calculates the system's free energy by integrating internal stress differences, which converge significantly faster with cell size compared to entropies and energies. This approach provides an ideal tool for testing various theoretical methods with different levels of precision, including *ab initio* calculations, force field models, and machine learning methods. Furthermore, the results may also serve as a benchmark for other free energy calculation methods.

Using these techniques, we hope to clarify the factors influencing the stabilities of Fe structures under core conditions and reach a unified consensus on the inner core crystalline structure. The rest of the paper is organized as follows: in Section 2 we introduce the techniques discussed and used in this study; Section 3.1 presents the stability of the bcc and fcc phases using the BP-TI method; Section 3.2 presents the results of free energy calculation for bcc, fcc and hcp Fe using two-phase thermodynamic (2PT) method, building on the results of the BP-TI calculations; in Section 3.3 we present their melting temperatures and discuss their possible occurrence in the core; Section 4 summarises the main findings and conclusions.

2. Methods

In this section, we introduce the techniques that will be used and discussed in this study. These include the two widely used EAM potentials and the AIMD method used in earlier work. The BP-TI method was previously used to evaluate the mechanical and thermodynamic stabilities of the bcc and fcc phases under IC conditions (Cui et al., 2013; Vočadlo, Wood, Gillan, et al., 2008). The energetics from the BP-TI method can be used to benchmark the free energy calculation. We also introduce the 2PT method that can treat both the solid and liquid states, allowing direct calculation of the free energies of diffusive system.

2.1 Bain path thermodynamic integration

The bcc↔fcc transformation can be continuously connected through a straightforward tetragonal path, known as the Bain path (Bain, 1924). This transformation is reversible and does not undergo any first-order phase transition. Therefore, in the spirit of the thermodynamic integration technique, the free energy differences can be calculated by integrating the reversible work required to drive the system from the reference state to the target state (Frenkel & Smit, 2002). Importantly, integrating along the Bain path corresponds to treating each point on the integral path as the reference frame for the subsequent point, thus eliminating the necessity for introducing additional reference systems. This characteristic is a key factor that enables the BP-TI method to achieve high-precision free energy calculations. Another significant advantage of this approach is that by integrating the work done by internal stresses, the convergence of these stresses is less dependent on the simulation cell size, thereby facilitating more rapid free energy convergence. Consequently, the mechanical and thermodynamic stability between bcc and fcc structures can be accurately determined by calculating the free energy difference during the bcc↔fcc phase transition.

The tetragonal strain involves distorting the bcc lattice by altering the c/a ratio while maintaining constant volume. Under this strain, both bcc and fcc structures can transform smoothly into one another, as there are two special cases of the body-centred tetragonal (bct) lattice for these structures: bcc corresponds to c/a = 1 and fcc to c/a = $\sqrt{2}$ (Stixrude & Cohen, 1995). To facilitate the integration, as outlined by Ozolins (2009), it is more convenient to

introduce a tetragonal distortion parameter τ that is equivalent to the previously mentioned c/a ratio. Then the bct lattice with a volume of a^3 can be described by the vectors **a** = ($a/\tau^{1/2}$, 0, 0), **b** = (0, $a/\tau^{1/2}$, 0), and **c** = (0, 0, $a\tau$). Clearly, $\tau = 1$ for the bcc structure, and $\tau = 2^{1/3}$ for the fcc structure. The work (w) associated with an infinitesimal tetragonal strain can be evaluated using

$$dw = f \cdot du = \sum_\alpha A_\alpha \sigma_{\alpha\alpha} du_\alpha \quad (1)$$

where f is the force, the summation is taken over $\alpha = x, y, z$. A_α represents the area of the faces of lattice cell perpendicular to the axial, $\sigma_{\alpha\alpha}$ is the principal component of stress tensor (the contributions of non-principal components $\sigma_{\alpha\beta}$ are 0 as they are perpendicular to the displacements of lattice faces), and du_α is the elastic displacement of lattice faces. Since $A_x = A_y = a^2\tau^{1/2}$, $A_z = a^2/\tau$, $u_x = u_y = a/\tau^{1/2}$, and $u_z = a\tau$, Equation (1) can be reduced to

$$dw = a^3[\sigma_{zz} - (\sigma_{xx} + \sigma_{yy})/2]/\tau\, d\tau \quad (2)$$

By taking the integral on both sides of Equation (2), we can obtain the Helmholtz free energy difference ΔF_V between the bct and bcc phases along the Bain path when we choose the bcc phase ($\tau = 1$) as the reference system:

$$\Delta F_V = \int dw = \int a^3[\sigma_{zz} - (\sigma_{xx} + \sigma_{yy})/2]/\tau\, d\tau \quad (3)$$

The Gibbs free energy of the bct lattice at reference pressure ($G_{\tau\to1}$) is calculated by integrating its equation of state:

$$G_{\tau\to1} = F_\tau + P_\tau V_1 + \int_{P_\tau}^{P_1} V\, dP \quad (4)$$

where F_τ is the Helmholtz free energy, P_τ is the pressure of the bct phase after applying the tetragonal strain, while P_1 and V_1 are the pressure and volume of the bcc phase, respectively. The third term V represents the equation of state of the bct lattice. The Gibbs free energy of the bcc phase (G_1) is expressed as:

$$G_1 = F_1 + P_1 V_1 \quad (5)$$

where F_1 is the Helmholtz free energy of the bcc phase. Then, the Gibbs free energy difference $\Delta G_{P\tau}$ between the bct and bcc phases along the Bain path at isobaric pressure can be evaluated by the following equation:

$$\Delta G_{P\tau} = G_{\tau\to 1} - G_1 = \Delta F_V + (P_\tau - P_1)V_1 + \int_{P_\tau}^{P_1} V\, dP \quad (6)$$

The shape and position of the free energy difference curves, ΔF_V and $\Delta G_{P\tau}$, decisively indicate the mechanical and thermodynamic stability of bcc and fcc structures.

2.2 Two-phase thermodynamic model

The 2PT model (Lin et al., 2003) was also employed to compute the entropy and free energy of the different Fe phases under inner core *P-T* conditions. This involves decomposing the Velocity Autocorrelation Function (VACF) and its associated Vibrational Density of States (VDoS) into a gas-like diffusion component and a solid-like vibrational component. The vibrational entropies of these two components were calculated using the Hard Sphere (HS) model and the Harmonic Oscillator (HQ) model, respectively (Desjarlais, 2013; Lai et al., 2012). The VACF (Φ), derived from the time evolution of velocities of *N* atoms, and its VDoS (*F*), obtained through the Fourier transform, are the two fundamental quantities in the 2PT model:

$$\Phi(t) = \left\langle \frac{\sum_{i=1}^{N} v_i(t)\cdot v_i(0)}{\sum_{i=1}^{N} v_i(0)\cdot v_i(0)} \right\rangle_{T_w} \quad (7)$$

$$F(v) = \int_0^\infty \Phi\,(t)\cos(2\pi v t)dt \quad (8)$$

where T_w represents the vibration time, *N* denotes the number of atoms, and $v_i(t)$ signifies the velocity of the *i*-th atom at time *t*. For systems like amorphous liquids or gases where low-frequency modes predominantly influence entropy, it is necessary to partition the total correlation function into solid-like and gas-like components:

$$\Phi(t) = (1 - f_g)\Phi_s(t) + f_g\Phi_g(t) \quad (9)$$

$$F(v) = (1 - f_g)F_s(v) + f_g F_g(v) \quad (10)$$

where F_g and F_s are the gas-like and solid-like contributions to the vibrational density of states, f_g is a fluidity factor to be determined. The vibrational entropy and other thermodynamic properties are then determined by weighting the solid-like and gas-like components with weighting functions:

$$S_{vib} = Nk_B \int_0^\infty [f_g F_g(v)\, W_g + (1 - f_g)F_s(v)W_s]dv \quad (11)$$

where W_s and W_g are the solid and gas entropy kernels, respectively. For exact methodology details, we refer to Wilson & Stixrude (2021) as we implemented their formulations of this method.

Compared to traditional free energy calculation methods, such as TI (Frenkel & Smit, 2002) and free energy perturbation (FEP) (Zwanzig, 1954), the 2PT model significantly simplifies the calculation of entropy by only requiring the post-processing of a single equilibrium MD trajectory. When the MD simulations are sufficiently large and long enough, a single equilibrium trajectory will contain ample information to fully characterize the entropy of the system (Wilson & Stixrude, 2021). This model has been widely adopted for determining thermodynamic properties across various complex systems (Hernandez et al., 2022; Sun et al., 2017), including those relevant to the Earth's inner core, such as pure Fe and FeH_x alloys with significant self-diffusion components (Yang et al., 2023).

2.3 EAM potentials

There are two EAM potentials developed by Alfè, Gillan, and Price (2002) (EAM-A hereafter) and Belonoshko et al. (2017) (EAM-B hereafter) that have been previously used to study the structure and properties of the Earth's core. In the present study they were used to calculate the thermodynamic properties with BP-TI and 2PT methods across the entire *P-T* range of the inner core. The total energy of the EAM potential has the form:

$$E_{tot} = \sum_i E_i \tag{12}$$

where E_i is the potential energy of atom *i*, which consists of two parts:

$$E_i = E_i^{\mathrm{rep}} + F(\rho_i) = \sum_j \epsilon \left(\frac{a}{r_{ij}}\right)^n - \epsilon C \rho_i^{1/2} \tag{13}$$

E_i^{rep} is a purely repulsive function of the interatomic distance r_{ij} and $F(\rho_i)$ is the embedded energy function accounting for the metallic bonding, with the densities $\rho_i = \sum_{j \neq i} \left(\frac{a}{r_{ij}}\right)^m$. The fitting parameters for EAM-A are: n = 5.93, ϵ = 0.1662 eV, C = 16.55, a = 3.4714 Å and m = 4.788 (Alfè, Gillan, and Price, 2002), and for EAM-B are: n = 8.7932, ϵ = 0.0220225 eV, C = 28.8474, a = 3.48501 Å and m = 8.14475 (Belonoshko et al., 2017). The differences between these two EAM potentials can be attributed to the variations in the temperatures and

configurations used during their fitting procedures. This may introduce different thermodynamic properties such as entropy, free energy and melting temperatures.

2.4 *Ab initio* calculations

We conducted *ab initio* molecular dynamics (AIMD) simulations and employed the BP-TI technique to examine the mechanical and thermodynamic stability of the bcc structure under tetragonal strain at ~330–360 GPa and 5000–7000 K. Density functional theory (Kohn & Sham, 1965) calculations were performed within the generalized gradient approximation (GGA) (Perdew et al., 1996) and the projector-augmented wave (PAW) method (Blöchl, 1994). The calculations were performed by using the Vienna *Ab initio* Simulation Package (VASP) code (Kresse & Furthmüller, 1996). To avoid any overlapping of core states at high pressures and temperatures, we treated fourteen electrons of Fe (Fe-$3p^6 3d^7 4s^1$) as valence. A single Gamma point with a cutoff energy of 550 eV was selected for supercells of 128 atoms (4 × 4 × 4 supercell of the cubic 2-atom box), consistent with the setup used in the previous study (Cui et al., 2013). A dense Gamma-centered 2 × 2 × 2 k-point mesh was adopted for static corrections on 40–100 snapshots extracted every 100–250 steps from the Gamma point MD simulations, and the final stress was obtained by averaging the corrected stresses to achieve higher accuracy in BP-TI calculations. The total energy was converged to 2×10^{-5} eV. These settings are sufficient to converge the stress and total energy within 0.1 GPa and 1 meV/atom, respectively (Table S1). Molecular dynamics trajectories were propagated in the NVT ensemble using the Nosé thermostat (Nosé, 1984) with a time step of 1 fs. The AIMD simulations lasted for 10 ps, and the last 80% were used for statistical sampling. The electronic population was accounted for through the Fermi–Dirac smearing approach (Mermin, 1965). Spin polarization was not considered since the thermal excitation of electrons would essentially destroy the residual magnetic moment at high temperatures (Sun et al., 2024; Vočadlo et al., 2003).

2.5 Computational details

Cell sizes up to 8192 atoms were tested for sufficient convergence using simulations based on the EAM potentials. For the BP-TI method, a system with a 1024-atom cell (8 × 8 × 8 supercell of the cubic 2-atom box) with a simulation duration of 100–200 ps, was sufficient to converge

the Helmholtz free energy difference ($\Delta F_{fcc-bcc}$) between the fcc and bcc phases to within 1 meV/atom (Figure S1). For the 2PT method this cell size, with an equilibrium duration of 60 ps, provided adequate convergence of the Gibbs free energy (G) of the bcc phase to within 2 meV/atom (Figure S2). For the fcc phase, a cell size of 864 atoms (6 × 6 × 6 supercell of the cubic 4-atom box) was suitable, while for the hcp phase, a slightly larger1200-atom cell (10 × 6 × 5 supercell of the 4-atom *C*-centred unit cell box) was used, ensuring consistent convergence levels for all free energy calculations using the 2PT model (Table S2).

To investigate whether diffusion affects the thermodynamic stabilities of the bcc phase, we tested different cell sizes from 1024 atoms (8 × 8 × 8 supercell) to 65536 atoms (32 × 32 × 32 supercell) at 360 GPa and 7000 K, with all simulations maintaining identical densities. Subsequently, the 2PT model was employed to calculate its vibrational entropy as a function of cell size. Additional MD simulations of 500 ps duration were performed to further examine how cooperative diffusion in the bcc phase depends on both system size and simulation time. To verify the phase state (solid or liquid) in the simulations, we retrieved the radial distribution function (RDF), the coordination number (CN), and the mean-square displacement (MSD) from a 15-ps segment of the equilibrium trajectory, with the results depicted in the supporting information Figures S3 and S4. Finally, the thermodynamic properties were evaluated using both the BP-TI technique and the 2PT model, based on these extensive MD simulations. The statistical error was assessed by the blocking method (Flyvbjerg & Petersen, 1989).

3. Results and Discussion

3.1. Mechanical and thermodynamic stabilities of bcc Fe from BP-TI method

As outlined in Section 2.1, the bcc↔fcc transformation can occur along the Bain path via tetragonal strain at constant volume, which does not involve any first-order phase transition. Therefore, the free energy change of this transformation can be determined by integrating the reversible work required to drive the system from the reference state to the target state. The mechanical stability of the bcc phase under tetragonal strain necessitates that its free energy must be at a local minimum. If this is not the case, the bcc phase will spontaneously convert to

fcc and as a result, cannot remain stable. It is important to note that some previous studies have focused on the hydrostatic nature of stresses to assess the mechanical stability of the bcc phase (Belonoshko et al., 2011; 2017; Vočadlo et al., 2003). However, hydrostatic equilibrium, as inferred from the stress analysis, does not necessarily correspond to a global free energy minimum. Instead, it may represent a local maximum, with the unit cell being unstable under a finite tetragonal strain (Godwal et al., 2015).

The stress anisotropy ($\sigma_{zz} - (\sigma_{xx} + \sigma_{yy})/2$) and the difference in integrated free energies (ΔF_V and $\Delta G_{P\tau}$) for various bct lattice structures along the Bain path at inner core *P*-*T* conditions, as determined from both EAM-A and EAM-B potentials, are illustrated in Figures 1 and 2, respectively. These two potentials show somewhat different behavior, as detailed in the following two paragraphs.

For the EAM-A potential, both the bcc (τ = 1) and fcc (τ =$2^{1/3}$) phases are found to be in a nearly hydrostatic state, exhibiting only minimal stress variations (Figures 1a and 1d). The stress anisotropy of the bct lattice initially increases from τ = 0.948 to τ = 1.052, then decreases to τ = 1.206, and subsequently increases again with further distortions. The integrated free energy changes suggest that the bcc phase would be mechanically stable, as its free energy is at a local minimum when integrating Equation (2) with respect to tetragonal strain. However, the fcc phase has a lower free energy than the bcc phase at temperatures of 5000 and 6000 K, and so the EAM-A potential predicts that the bcc phase would be metastable under IC conditions relative to fcc. Moreover, the temperature appears to enhance the stability of the bcc phase, while pressure tends to reduce it. The almost overlapping ΔF and ΔG can be attributed to the small volume changes (i.e., the equation of state) during the bcc↔fcc transformation. Notably, at 7000 K, a shift in the relative stability between the bcc and fcc phases becomes evident, as indicated by the positive values of both the ΔF and ΔG. However, according to established melting curves (Alfè, 2009; Anzellini et al., 2013; Sun et al., 2023), Fe is expected to melt at this elevated temperature. The persistence of solid-like states in BP-TI calculations at 7000 K reflects the superheating phenomenon in MD simulations, where crystals can remain metastable above their equilibrium melting temperature until sufficient fluctuations or defects trigger melting. Consequently, the free-energy values obtained for both bcc and fcc at 7000 K

correspond to metastable solid-like configurations sustained under superheating conditions.

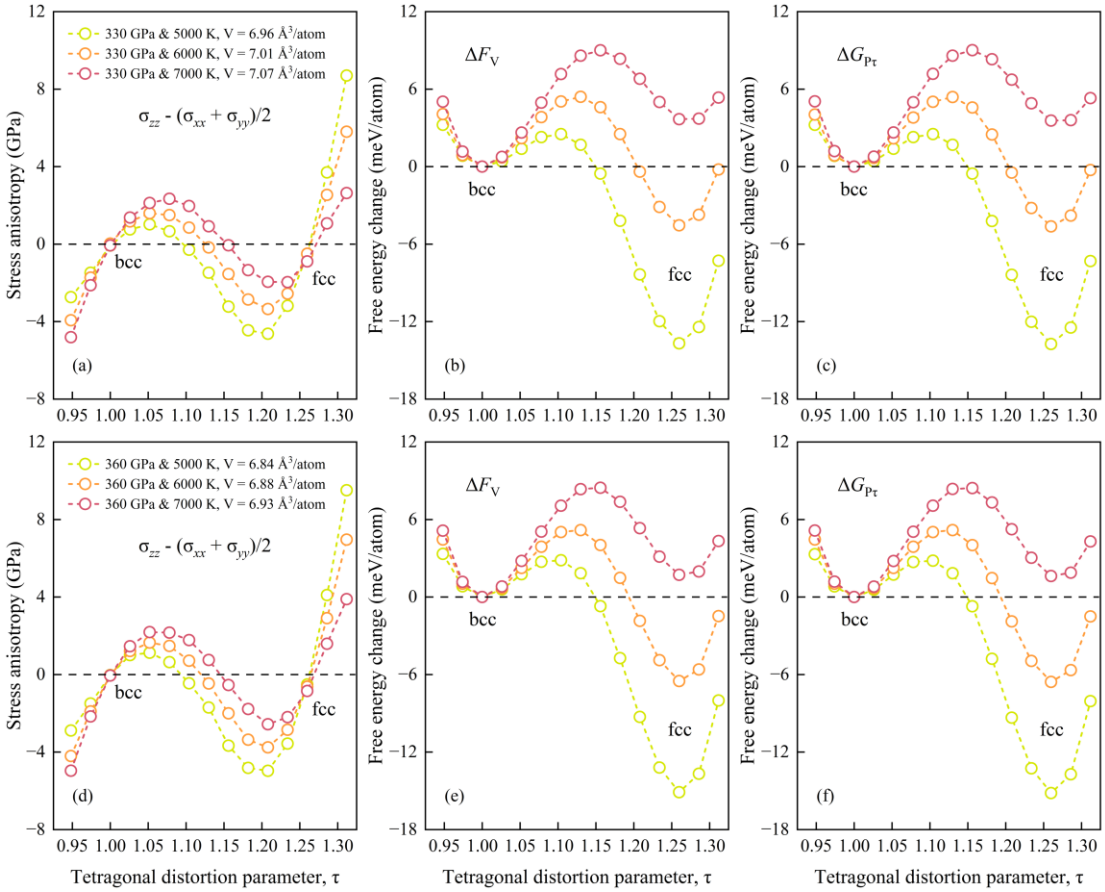

Figure 1. Stress anisotropy (a, d) and integrated free energy change (b-c, e-f) of the bct lattice with respect to tetragonal strain at inner core *P-T* conditions (330 GPa upper, 360 GPa lower), based on the EAM-A potentials (Alfè, Gillan, & Price, 2002). Uncertainty in stress anisotropy is typically less than 0.1 GPa, which is smaller than the symbol size; while uncertainty in the free energy difference accounts for both the error in stress tensor calculations and the integration process, which is less than 2 meV/atom in all cases. The dashed curves serve as guides for the eyes only.

Figure 2 shows the results from the EAM-B potential. At 5000 K, the stress anisotropy of the bct lattice initially decreases from $\tau = 0.948$ to $\tau = 1.182$ before increasing with further distortions. At 6000 K, the stress anisotropy firstly decreases from $\tau = 0.948$ to $\tau = 0.974$ and then increases to $\tau = 1.026$. As shown in Figures 2b–2c and 2e–2f, the free energy of the bcc phase resides at a local minimum, indicating its mechanical stability. At high temperatures of 7000 K, the stress anisotropy and integrated free energy changes for the bct lattice exhibit similar behavior to that observed using the EAM-A potentials, in which the energy of the bcc

phase lies clearly at a local minimum, while the fcc phase consistently occupies the global minimum. Consequently, the EAM-B potential also predicts that the bcc phase would be metastable under IC conditions relative to fcc. Note that the abrupt change in stress anisotropy (i.e., $\tau = 1.104$ and 1.156 at 5000 K) observed with the EAM-B potentials corresponds to the formation of a stacking fault on the (101) plane of the bct lattice, with the stacking-fault direction oriented diagonally across this plane (from top left to bottom right), as confirmed by direct visual inspection of the MD trajectories (Figure S5).

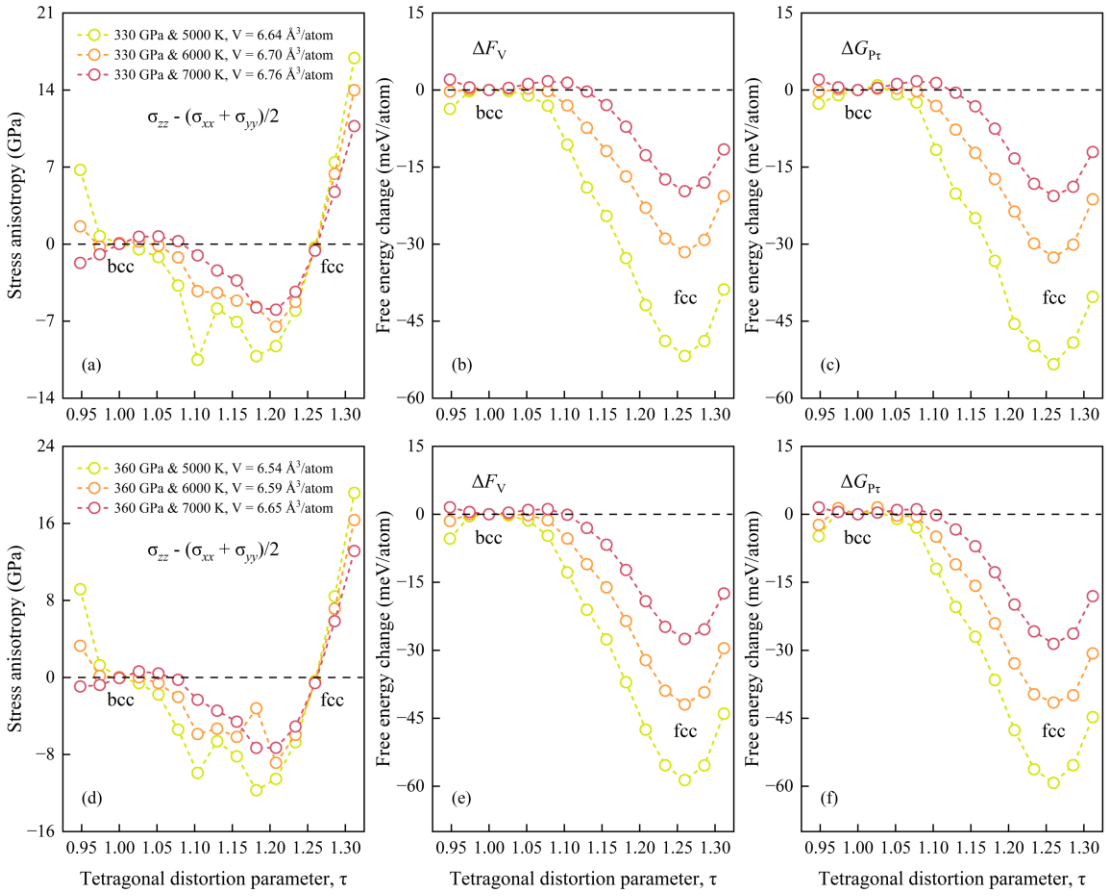

Figure 2. Stress anisotropy (a, d) and integrated free energy change (b-c, e-f) of the bct lattice with respect to tetragonal strain at inner core *P-T* conditions (330 GPa upper, 360 GPa lower), based on the EAM-B potentials (Belonoshko et al., 2017). Uncertainty for the stress anisotropy is typically less than 0.1 GPa, while uncertainty for the free energy difference is less than 2 meV/atom in all cases.

Recent studies have reported that the bcc phase can remain stable under conditions involving large cell sizes ($N \geq 1024$ atoms) and extreme *P-T* conditions (360 GPa and 7000 K) (Belonoshko et al., 2017). In contrast, our BP-TI calculation results based on various EAM

potentials demonstrate that bcc Fe is metastable under IC conditions with respect to fcc. To further validate the results obtained from the EAM potentials, we carried out AIMD simulations using the same BP-TI techniques at comparable *P-T* conditions. Although with shorter simulation times of 10 ps and smaller system sizes containing 128 atoms, the AIMD results confirm that bcc Fe remains mechanically stable but thermodynamically less stable even up to temperatures of 7000 K (Figure 3), generally consistent with the EAM predictions. Note that at lower temperatures of 5000 K, however, the bcc phase lies near an energy maximum and does not exhibit mechanical stability (Figure 3 and Figure S6). This becomes more apparent in the stress anisotropy, where stability is characterized by negative values at $\tau < 1$ and positive values at $\tau > 1$. Nevertheless, considering that inner core temperatures would exceed 5000 K, both EAM and AIMD calculations now consistently indicate that bcc holds a subtle mechanical stability under IC conditions (Figures 1–3). These findings differ from earlier *ab initio* simulations (Cui et al., 2013; Godwal et al., 2015), where the relatively large distortions applied (e.g., $\tau = 0.052$) may have overlooked the subtle mechanical stability of bcc, particularly at lower temperatures (5000–6000 K). This comparison underscores the importance of employing smaller distortion steps in BP-TI calculations to more accurately capture the weak mechanical stability of the bcc phase under IC conditions (Figure 3 and Figure S6). In addition, our convergence tests indicate that while a Gamma-point mesh was employed in Cui et al. (2013), denser k-point sampling is required to achieve higher accuracy in BP-TI calculations. Our results are consistent with more recent studies at 330–360 GPa (Zhang et al., 2025) and at 400 GPa (Ghosh et al., 2023; Li & Scandolo, 2024a).

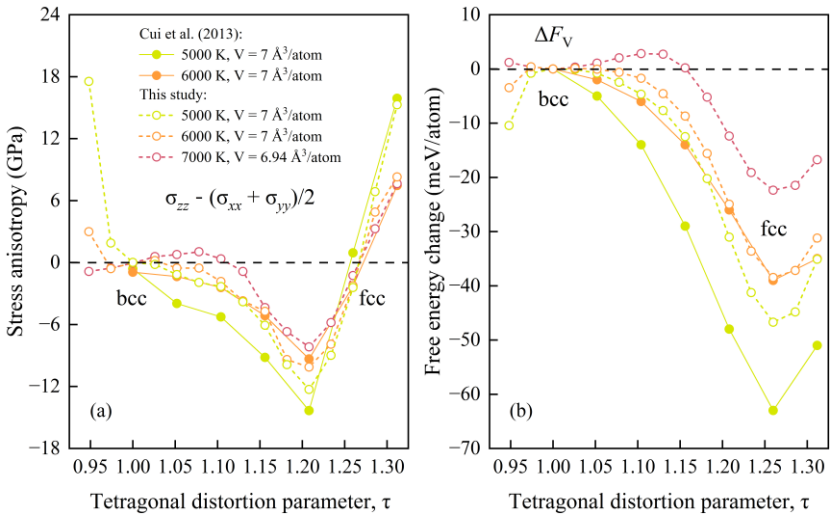

Figure 3. Stress anisotropy (a) and integrated free energy change (b) of the bct lattice with respect to tetragonal strain at inner core *P-T* conditions, based on *ab initio* calculations. The statistical uncertainty in stress anisotropy, evaluated using the blocking method, is typically less than 0.5 GPa, corresponding to an uncertainty in the free energy difference of no more than 5.5 meV/atom.

We also tried to use available Machine Learning (ML) potentials to assess the mechanical and thermodynamic stabilities of the bcc phase. The ML potential developed by Jana & Caro (2023) is suggested to be suitable for simulating Fe phases under IC conditions. However, our calculations show that this ML potential is unable to simulate the bcc↔fcc phase transition along the Bain path, as the simulated structures melted at 6000 K (Figure S7), as well as premelting at 5000 K (Figure S8). As this ML potential was trained on *ab initio* results, it should have the same melting temperature as the *ab initio* simulations. Furthermore, other existing ML potentials have not been publicly released, and discrepancies persist among these potentials in simulating Fe properties, such as the melting temperature (Li & Scandolo, 2024b; Wu et al., 2024; Yuan & Steinle-Neumann, 2023; Zhang et al., 2020). This highlights the critical need for the development of ML-based potentials suitable for long-duration and large-scale MD simulations of core Fe alloys.

In summary, we conclude that both EAM potentials and *ab initio* simulations show that the bcc phase is mechanically stable, but remains thermodynamically less stable than the fcc phase under IC conditions. As it is well established that the fcc phase is less stable than the hcp phase (Li & Scandolo, 2024a; Stixrude, 2012; Vočadlo et al., 2000; 1999), it is clear that bcc cannot be the stable phase of pure Fe under core conditions. Nevertheless, it has been suggested that diffusion may stabilise the bcc phase, and that this is only seen in simulations with large numbers of atoms. We examine that next.

3.2. Thermodynamic stabilities of Fe structures from 2PT free energy calculations

3.2.1 Size effects and self-diffusion

The cooperative diffusion mechanism has been proposed to stabilise the bcc phase of Fe under IC conditions, with large systems being necessary for this stabilisation (Belonoshko et al., 2017). Their analysis of configurations and trajectories unveiled diffusive processes that may

contribute to entropy, thereby stabilising the bcc phase (Figure 4). More importantly, it was argued that such diffusion mechanisms cannot be supported in small systems without destroying their structure, emphasising the significant size dependence in the stability of the bcc phase. However, a subsequent study by Schultz et al. (2018) argued that the entropy of bcc Fe exhibits no system size-dependent anomalies, based on their extensive TI thermodynamic calculations. They claimed the accurate free energy calculations for this system can be computed using *ab initio* methods without the need for excessively large atomistic models. Although both studies used identical EAM potentials, cell sizes, and *P*-*T* conditions, they differed in the approaches employed to determine the entropy and free energy of the system. Schultz et al. (2018) argued that the VACF method used in Belonoshko et al. (2017) does not accurately predict free energies for systems with self-diffusion. This challenges the notion that prohibitively large systems are necessary for proper simulations of bcc Fe. Therefore, further clarification is required regarding the size dependence on the stability of the bcc phase to gain a clear understanding of the inner core structures.

Here, we used the 2PT model to examine the discrepancies of size dependence on the bcc phase stabilities, with results presented in Figure 4. The system size modelled for the bcc phase ranged from 1024 to 65536 atoms, consistent with the sizes used in the previous study (Schultz et al., 2018). For the hcp phase under IC conditions, simulations were conducted with system sizes ranging from 256 to 4000 atoms, as previous work has shown that no obvious system-size anomalies in entropy with the system containing more than 1000 atoms (Belonoshko et al., 2017; Schultz et al., 2018; Sun et al., 2018). Our results reveal that the entropy of the bcc phase exhibits negligible size dependence, maintaining a nearly constant value as the system size increases. This can be confirmed from the convergence of the total VDoS versus simulation cell size (Figure S9). The entropy calculated using the 2PT model is systematically larger than that obtained from the TI method of Schultz et al. (2018) (Figure 4). This is likely due to the use of EAM potential. Theoretically, the energy difference between two structures should be identical from different free energy calculation methods. However, the potential may not be well trained to provide accurate description of the phase space explored during simulations. Therefore, variations in methods and integration paths in TI calculations could result in energy

shifts. Nevertheless, the entropy difference between the bcc and hcp phases ($\Delta S_{bcc-hcp}$) is estimated to be ~1.2 J/mol/K (0.1443 k_B/atom), which is very close to the value of ~1.3 J/mol/K (0.1564 k_B/atom) reported by Schultz et al. (2018) in their TI calculations. Such an entropy difference is not sufficient to render the bcc structure thermodynamically more stable than the hcp structure, as stability would require $\Delta S_{bcc-hcp}$ > 1.52 J/mol/K (0.1831 k_B/atom). This finding is further corroborated by Li & Scandolo (2024a), who, based on the deep-learning potential calculations, suggested that the self-diffusion mechanism is inadequate to stabilise bcc Fe thermodynamically over other competing phases.

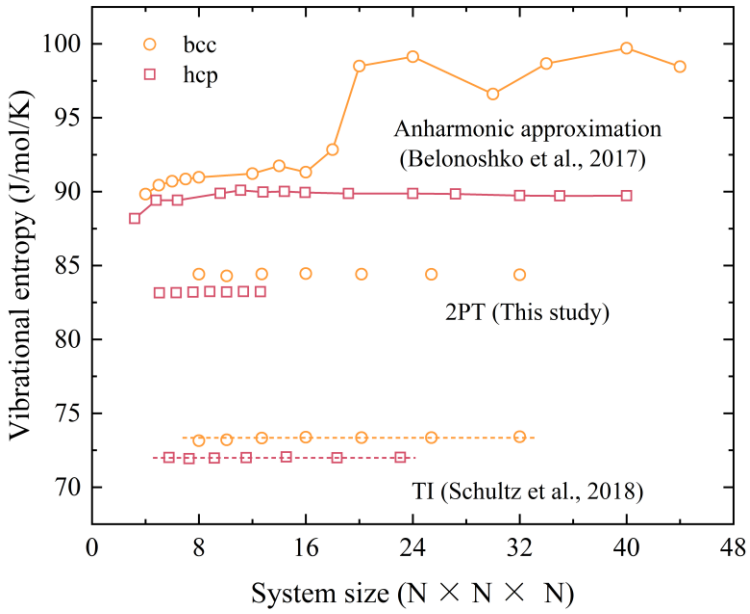

Figure 4. Size dependence of entropy of the bcc and hcp phases computed at 360 GPa and 7000 K using the EAM-B potentials, compared with results from the literature that employed the same potentials. System size is provided in N×N×N unit cells, where each unit cell contains 2 atoms for the bcc phase and a 4-atom *C*-centred unit cell for the hcp phase (normalized to 2 atoms for unified representation). For N = 32, the system consists of 65536 atoms. Although diffusion is observed in large supercell configurations (e.g., with 32768 and 65536 atoms), the entropy difference of the bcc phase is very small and nearly constant, consistent with the TI results reported by Schultz et al. (2018). Dashed lines are the linear fit to the data points.

Although our MD trajectory analysis reveals some diffusion in large bcc supercell configurations, as indicated by the MSDs depicted in Figure 5, the calculated entropy does not exhibit a rapid increase as observed by Belonoshko et al. (2017). In their study, cooperative

diffusion was found to significantly contribute to low-frequency modes, resulting in a substantial rise in entropy within the bcc phase. However, Schultz et al. (2018) argued that diffusion *per se* does not directly contribute to the free energy, which is an equilibrium thermodynamic quantity that can be defined and computed without any reference to dynamic behavior. They proposed that anomalous entropy scaling can be rigorously demonstrated through precise free energy calculations using various simulation methods, and the presence or absence of diffusion has no effect on the entropy. In contrast, Li & Scandolo (2024a) contend that the existence of self-diffusion invalidates direct TI approaches for free energy calculations by using ideal or Einstein crystals as references. Reconciling these divergences calls for diffusion-aware reference models or advanced sampling methods such as metadynamics or Monte Carlo dynamics that can accommodate atomic mobility without compromising thermodynamic rigor. While the self-diffusion in bcc phase may contribute to entropy, our current study, along with previous works (Li & Scandolo, 2024a; Schultz et al., 2018), suggests that such contributions are likely limited and not scaled significantly with cell size.

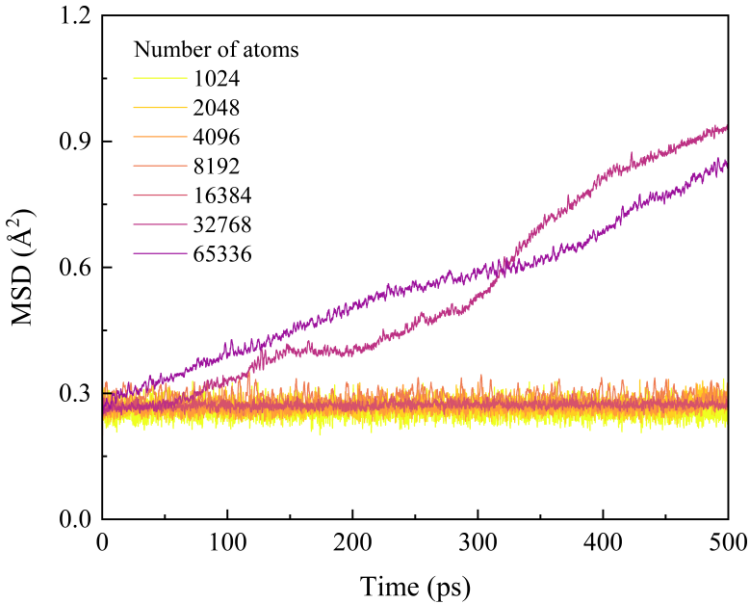

Figure 5. MSDs for different cell sizes in the bcc phase at 360 GPa and 7000 K based on the EAM-B potentials. Self-diffusion is observed in configurations with 32,768 and 65,536 atoms, while smaller systems show no obvious diffusion. This indicates that diffusion is generally more prevalent in larger systems.

3.2.2 Corroborating the BP-TI results with 2PT model

In Section 3.1, we examined the mechanical and thermodynamic stabilities of the bcc phase under tetragonal strain using the TI techniques, incorporating both semi-empirical EAM potentials and *ab initio* simulations. Building on the convergence accuracy of the BP-TI free energy calculations, we now extend our analysis by performing additional thermodynamic calculations using the 2PT model, after clarifying the size effect on the stability of the bcc structure. This approach aims to corroborate the BP-TI results and is expected to be consistent with our previous findings.

The VACF and its associated VDoS for the bcc and fcc phases under relevant *P-T* conditions are displayed in Figures 6 and 7, respectively. The reduced number of distinct peaks in the VACF of the fcc phase at 7000 K, as obtained from the EAM-A potentials, suggests that the phase has undergone melting (Figure 6c). This is further supported by the presence of finite VDoS (due to diffusive modes) at zero frequency (Figure 7c). In contrast, when employing the EAM-B potentials, the fcc phase still retains solid phase characteristics, with more peaks in the VACF and its VDoS tends towards zero at the long wavelength limit (Figure 6d). In the case of the bcc phase, it maintains a solid state regardless of the EAM potentials used, as evidenced by the VACF and VDoS shown in Figures 7a and 7b. However, it is worth noting that there is a very slightly diffusive behavior in the bcc phase at 7000 K when using the EAM-A potentials, as indicated by slow, stair-like features in its MSD as the simulation time increases (Figure S4).

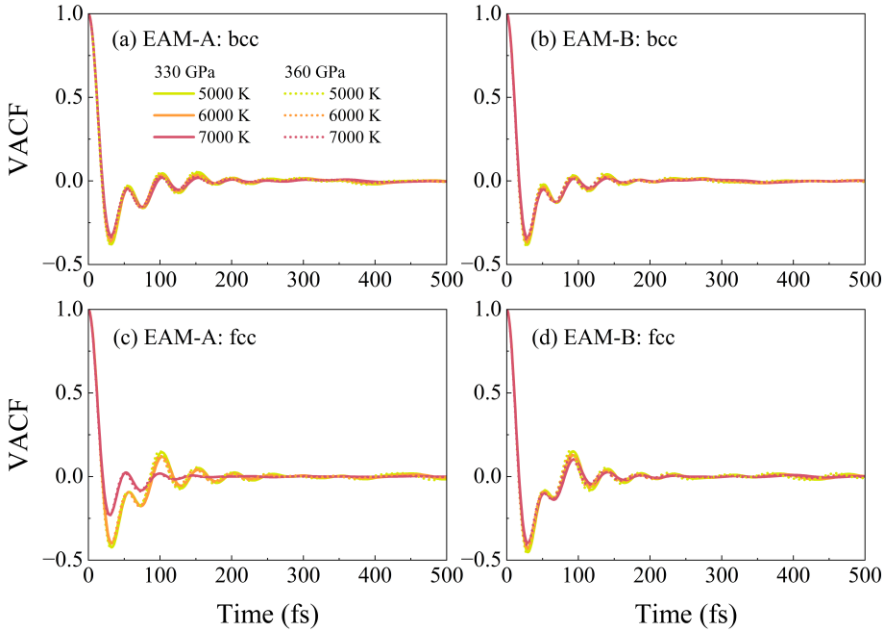

Figure 6. Velocity autocorrelation functions for the bcc (a-b) and fcc (c-d) phases of Fe at different *P-T* conditions as indicated in the legend. Solid lines represent the data at 330 GPa, while dot lines correspond to the data at 360 GPa.

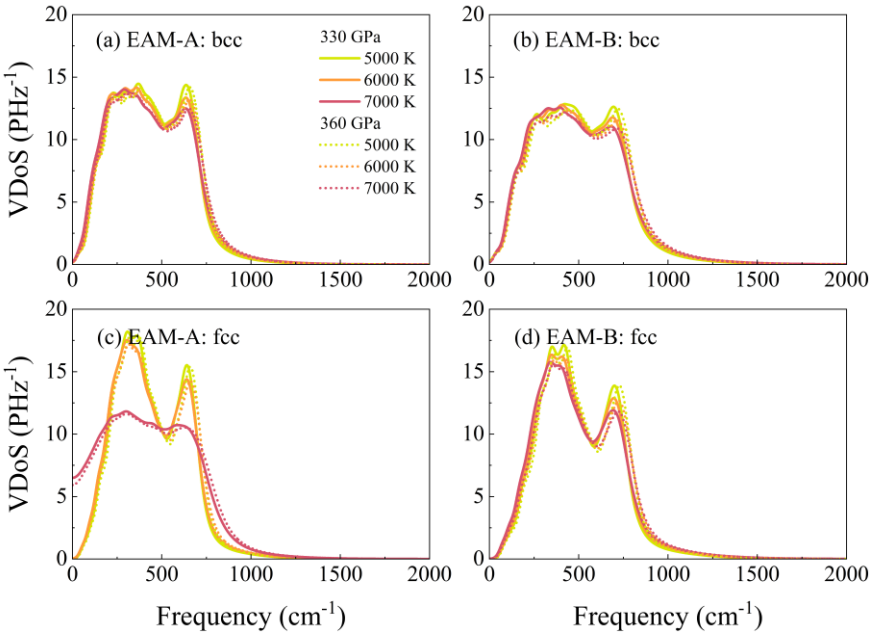

Figure 7. The total vibrational density of states of the bcc (a-b) and fcc (c-d) Fe under different *P-T* conditions. Solid lines represent the data at 330 GPa, while dot lines correspond to the data at 360 GPa.

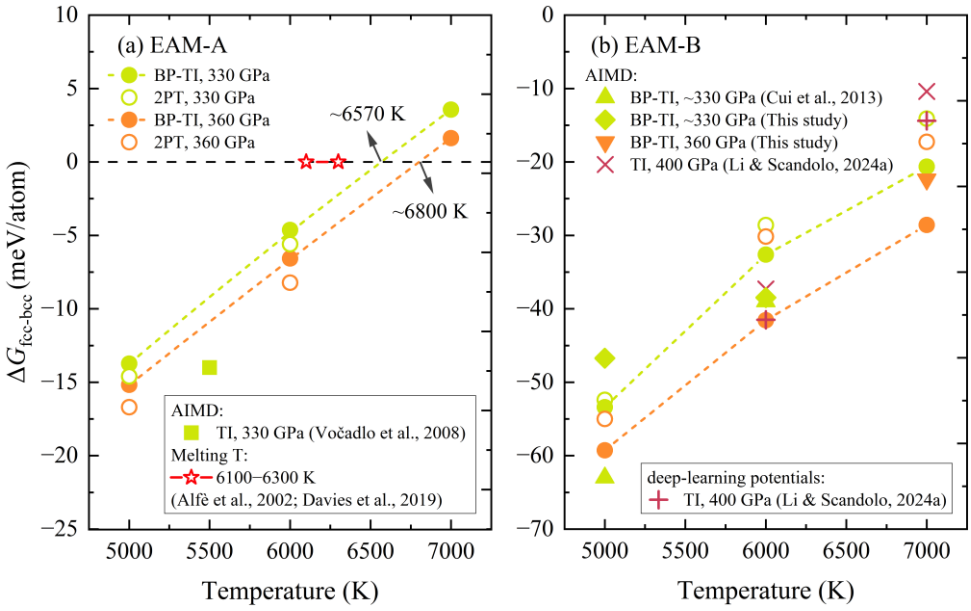

Figure 8. Free energy changes between the fcc and bcc phases of Fe under IC *P-T* conditions based on different force fields and methods. Solid and open circles denote the results from BP-TI and 2PT, respectively. Green represents calculations at 330 GPa while orange represents results at 360 GPa. The square corresponds to *ab initio* data reported by Vočadlo, Wood, Alfè, and Price (2008). Upper triangles

indicate *ab initio* results from Cui et al. (2013), while lower triangles represent the *ab initio* results of this study. Additionally, the *ab initio* and deep-learning potential data (shown in purple) explored at 400 GPa by Li & Scandolo (2024a) are included for comparison. The melting temperature of bcc Fe (indicated in red) is sourced from Alfè, Gillan, and Price (2002) and Davies et al. (2019).

Figure 8 illustrates the free energy changes between the fcc- and bcc-Fe ($\Delta G_{\mathrm{fcc-bcc}}$) under IC *P-T* conditions, as evaluated through the 2PT model. Remarkably, the results derived from the 2PT model demonstrate robust agreement with those obtained from the BP-TI approach, particularly notable in the EAM-A potentials (Figure 8a), where the discrepancy is less than 2 meV/atom. Furthermore, these results are in good agreement with previous *ab initio* assessments conducted at ~330 GPa and 5500 K using the coupling parameters TI method (Vočadlo, Wood, Alfè, & Price, 2008), which shows a disparity of only ~4 meV/atom. For the EAM-B potentials (Figure 8b), although marginally larger, the difference remains within 7 meV/atom up to temperatures of 7000 K, and the results align well with the *ab initio* computations reported by Cui et al. (2013) as well as close to the recent calculations conducted at 400 GPa based on the *ab initio* and deep-learning potentials (Li & Scandolo, 2024a).

According to the EAM-A potentials, the temperatures required to stabilise the bcc phase over fcc phase of Fe at 330 and 360 GPa are estimated to be ~6570 and ~6800 K, respectively (Figure 8a). However, using the same EAM potentials, Alfè et al. (2002a) and Davies et al. (2019) determined the melting temperatures of the bcc phase under IC pressure conditions to be in the range of ~6100–6300 K, which are lower than the stabilisation temperatures predicted by the EAM-A potentials. For the EAM-B potentials, the necessary stabilisation temperatures exceed 8000 K (Figure 8b). Therefore, while temperature can stabilise the bcc phase, it remains far from completely stable across the entire range of IC temperatures, as the required stabilisation temperatures exceed the melting temperature of Fe under these conditions, irrespective of whether EAM-A or EAM-B potentials are employed.

3.3. Melting temperatures of Fe structures and the inner core

It is well established that the fcc structure is thermodynamically less stable than the hcp structure under IC conditions, primarily due to its larger thermal pressure term (Stixrude, 2012;

Vočadlo et al., 2000; 1999). More recent work by Li & Scandolo (2024a), using *ab initio* and deep-learning interatomic potential for Fe at extreme conditions, further supports this hypothesis, although the mechanical stability of the bcc phase under tetragonal strain based on this deep-learning interatomic potential has not been clarified. While the observed *P*-wave anisotropy in the inner core has been attributed to the fcc structure (Vočadlo, Wood, Alfè, & Price, 2008), this alone cannot completely account for the complex anisotropy of the inner core, especially when compared to the hcp and/or bcc structures (Mattesini et al., 2010; Romanowicz et al., 2016; Tateno et al., 2010). Consequently, the fcc structure is not included in this section and the focus is solely on the bcc, hcp, and liquid phases.

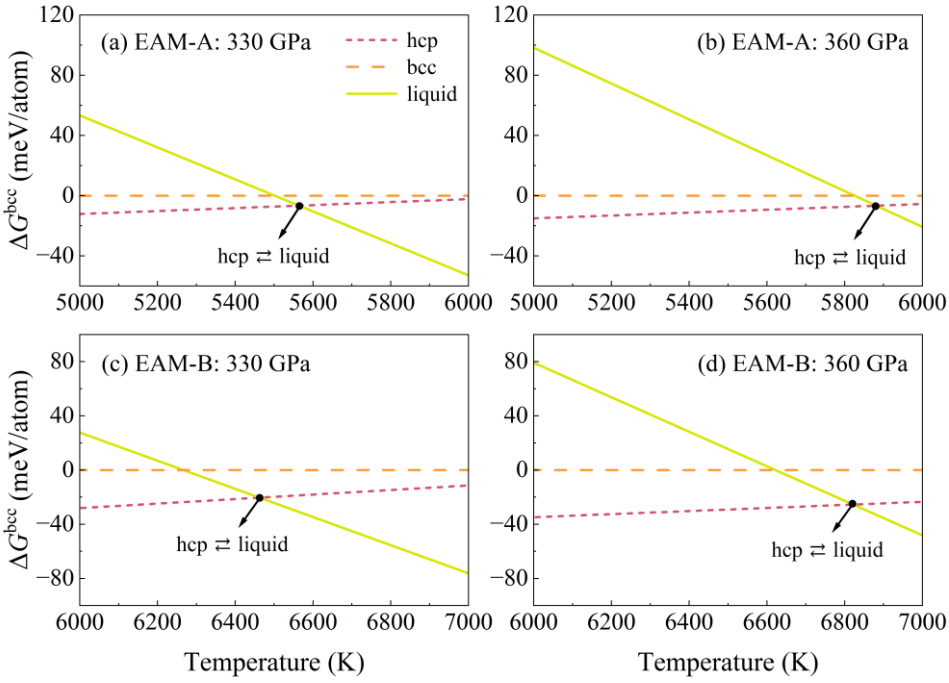

Figure 9. Free energy differences referenced to bcc Fe at 330 and 360 GPa near the melting temperatures. The black dots indicate the phase transition from hcp to liquid.

We calculated the melting temperatures of different Fe structures using the 2PT model based on the EAM potentials by comparing their absolute Gibbs free energies with those of the liquid phase. The VACF and its associated VDoS for the hcp and liquid phases at inner core *P-T* conditions are shown in Figures S10 and S11, respectively. The calculated free energy difference relative to the bcc phase is shown in Figure 9. The free energy difference between hcp and bcc using EAM-A is minimal, generally less than 15 meV/atom (with bcc being higher) under relevant IC conditions. This difference increases when employing EAM-B, reaching ~35

meV/atom, which is close to the recent value of ~46 meV/atom (calculated using TI) based on deep-learning potentials at 400 GPa and 6000–7000 K (Li & Scandolo, 2024a). However, the values obtained from EAM potentials are lower than those from *ab initio* calculations, which yield ~60 meV/atom from TI (González-Cataldo & Militzer, 2023) and 170–270 meV/atom from the quasiharmonic approximation, both at 330–360 GPa and 6000 K (Zhang et al., 2025). These discrepancies most likely arise from differences in the employed potentials and free-energy calculation methods.

For the EAM-A potentials, the calculated melting temperatures are ~5500 K for bcc and ~5565 K for hcp at 330 GPa, while ~5825 K for bcc and ~5900 K for hcp at 360 GPa (Figures 9a and 9b). Using the EAM-B potentials, the melting temperatures are determined to be ~6265 K for bcc and ~6460 K for hcp at 330 GPa, while ~6620 K for bcc and ~6820 K for hcp at 360 GPa (Figures 9c and 9d). Generally, a solid phase with the highest melting temperature is considered the most stable phase, while other solid phases remain metastable near the melting temperature. It is evident that the hcp phase consistently exhibits a higher melting temperature than the bcc phase, suggesting it should be the most stable phase in the Earth's inner core. Furthermore, the melting temperature of Fe derived from the EAM-B potentials is ~750–900 K higher than that obtained based on the EAM-A potentials. The different fitting procedures in temperatures and configurations may explain this discrepancy (Alfè, Gillan, & Price, 2002; Belonoshko et al., 2017).

The melting temperatures of the bcc and hcp phases obtained from the EAM potentials are compared with available literature values (Figure 10). The data for the hcp phase is abundant, while the bcc phase has a more limited set of values. One *ab initio* data point for the bcc melting point comes from Bouchet et al. (2013), in which the calculation was performed with a 256-atom solid-liquid coexistence (SLC) cell, leading to considerable uncertainties in both pressure and temperature. Another *ab initio* estimate is from Sun et al. (2023), where they determined an *ab initio* melting point using PAW8 and PAW16 pseudopotentials. A more recent data point of ~6480 K for bcc Fe is reported by Wu et al. (2024), derived from the deep potential (DP) model. Our results for the bcc phase, based on the EAM-B potentials, are in good agreement with these studies (Bouchet et al., 2013; Sun et al., 2023; Wu et al., 2024), but ~450 K higher

than that of Li & Scandolo (2024a) based on their DP determinations. This discrepancy implies that the current DP model for Fe at IC conditions from different groups still exhibits some inconsistencies (Li & Scandolo, 2024a; Wu et al., 2024). The largest deviation is seen in the bcc phase from Belonoshko, Fu, and Smirnov (2022), showing a melting temperature ~685 K higher than our EAM-B value at 360 GPa. This divergence is particularly notable as it suggests the melting temperature of the hcp phase is much lower than that of the bcc phase at the inner core center. Such deviation could be attributed to the employed semi-empirical potential, which was fitted to 0 K DFT results, and the calculated free energy contained an *ad hoc* correction for the electronic entropy effects (Belonoshko et al., 2021; Belonoshko, Fu, & Smirnov, 2022).

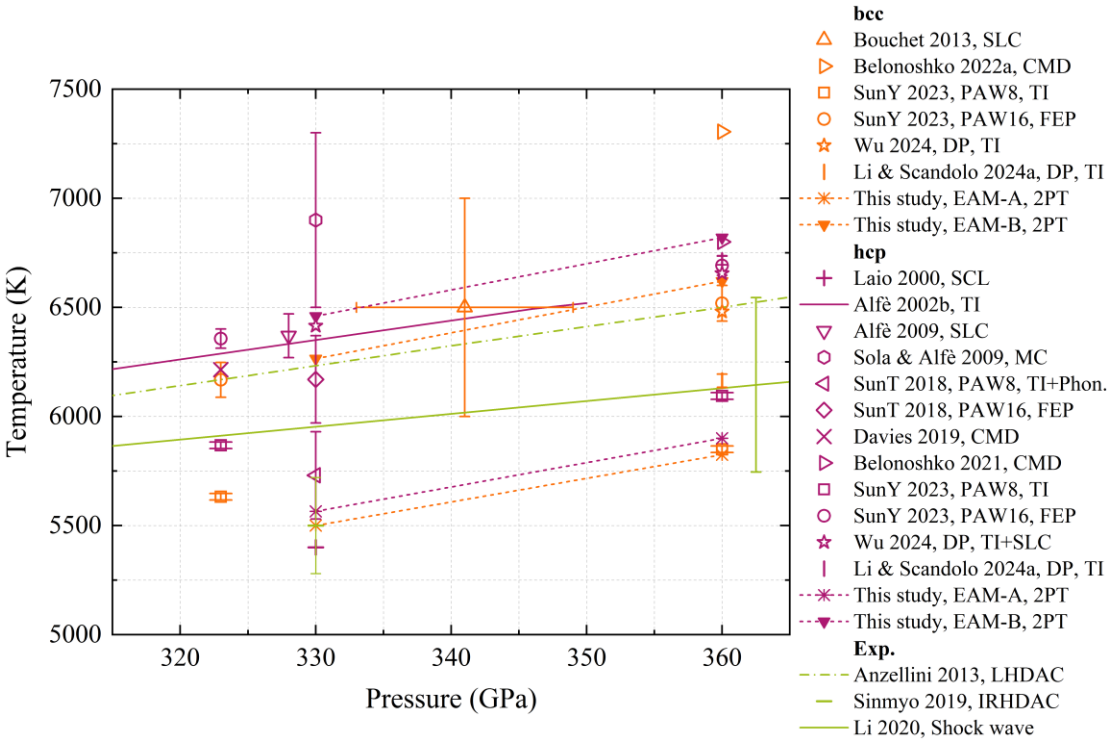

Figure 10. Melting temperatures of the bcc (orange) and hcp (red) phases determined by the 2PT model with EAM potentials, and data from literature is provided for comparison. Literature sources include *ab initio* SLC simulations by Laio (2000), Alfè (2009), and Bouchet et al. (2013); *ab initio* TI and SLC simulations by Alfè, Price, and Gillan (2002); *ab initio* TI, phonon quasiparticle, and FEP calculations by Sun et al. (2018; 2023); Monte Carlo (MC) simulations by Sola & Alfè (2009), and classical MD simulations by Davies et al. (2019) and Belonoshko et al. (2021) and Belonoshko, Fu, and Smirnov (2022). Additionally, melting temperatures predicted by the DP model are from Wu et al. (2024) using TI and SLC simulations, and Li & Scandolo (2024a) using TI methods. Experimental melting data (green)

658 are taken from Anzellini et al. (2013), Sinmyo et al. (2019) and Li et al. (2020), based on the extrapolated
659 data from DAC and shock wave experiments, respectively.

660 Our calculated melting temperature for the hcp phase with EAM-A potentials at 330 GPa is
661 reasonably consistent with the data of Sun et al. (2018) using the PAW8 pseudopotential within
662 uncertainties. This data also agrees with recent shock wave experimental results from Li et al.
663 (2020) at 360 GPa, within their margin of error. Note that using the same EAM potential, a
664 higher melting temperature (~6215 K) of the hcp phase at 323 GPa was predicted through SLC
665 simulations (Davies et al., 2019; Gao et al., 2025). The difference in methods for determining
666 the melting point may account for this discrepancy, as the SLC simulations may be susceptible
667 to superheating, leading to an overestimation of the melting point. Nevertheless, the difference
668 in melting temperature between hcp and bcc is nearly the same for both methods: ~70 K (with
669 hcp being higher) for the SLC simulations from previous studies (Davies et al., 2019; Gao et
670 al., 2025), and ~65 K for the free energy calculations in the current work. On the other hand,
671 our melting temperature from the EAM-B at 330 GPa aligns well with the *ab initio* 980-atom
672 SLC simulations conducted by Alfè (2009), and is also close to the values from the DP model
673 determined through TI and SLC by Wu et al. (2024). At the higher pressure of the inner core
674 center (~360 GPa), our EAM-B result is nearly identical to the data examined recently by
675 Belonoshko et al. (2021), with a difference of only ~20 K. Overall, both EAM potentials predict
676 a higher melting temperature for hcp than bcc, indicating that hcp is more stable, which is
677 consistent with previous studies (Li & Scandolo, 2024a; Sun et al., 2023; Wu et al., 2024).
678 These results establish a clear distinction in the relative stability between the hcp and bcc phases
679 under the same level of calculation accuracy.

680

681 ## 4. Conclusions

682 We have investigated the mechanical stability of the bcc structure under tetragonal strain by
683 employing the high-precision BP-TI technique. Our results, derived from both EAM potentials
684 and *ab initio* simulations, demonstrate that the bcc phase is mechanically stable but
685 thermodynamically less stable relative to fcc under IC conditions, with this metastability being

686 independent of the simulation cell size. Thermodynamic calculations based on the 2PT model
687 further corroborate these results. Although some self-diffusion is observed in bcc cells at
688 elevated temperatures, its contribution to entropy is found to be negligible, which contradicts
689 prior claims suggesting a significant entropy contribution from this diffusion. Furthermore, our
690 melting point calculations reveal that, under IC pressure conditions, the hcp phase consistently
691 exhibits a higher melting temperature than the bcc phase. This suggests that the hcp phase is
692 the most stable phase for pure Fe under these extreme conditions, reinforcing previous
693 methodologies and conclusions regarding the stability of Fe in the Earth's inner core.

694 Nevertheless, the free energy difference between the hcp and bcc phases is minimal, only on
695 the order of tens of meV/atom, which is comparable to the thermal energy ($k_B T$) per atom at
696 room temperatures. Furthermore, alloying with other elements, such as Ni, Si, S, and H, may
697 influence inner core phase stabilities and crystallization processes. Therefore, further
698 investigation is essential to better understand the combined impact of alloying elements on
699 phase behavior and to refine our knowledge of the structures and properties of the Earth's
700 interior.
701

Conflict of Interest

The authors declare no conflicts of interest relevant to this study.

Acknowledgments

We acknowledge three anonymous reviewers for their constructive comments and the editor for handling this manuscript. This work is financially supported by the National Natural Science Foundation of China (No. 42322201). Y. Li thanks the support from the CAS Hundred Talents Program. H. Yang acknowledges the support from the China Postdoctoral Science Foundation (2024M763142) and the Postdoctoral Fellowship Program (Grade C) of China Postdoctoral Science Foundation (GZC20241626). Calculations were conducted at the Supercomputing Center of the University of Science and Technology of China.

Open Research

Data Availability Statement

The data files used in this paper are available at (Yang et al., 2025).

References

Alfè, D. (2009). Temperature of the inner-core boundary of the Earth: Melting of iron at high pressure from first-principles coexistence simulations. *Physical Review B*, *79*(6), 060101. https://doi.org/10.1103/PhysRevB.79.060101

Alfè, D., Gillan, M. J., & Price, G. D. (2002). Complementary approaches to the ab initio calculation of melting properties. *The Journal of Chemical Physics*, *116*(14), 6170–6177. https://doi.org/10.1063/1.1460865

Alfè, D., Price, G., & Gillan, M. (2002). Iron under Earth's core conditions: Liquid-state thermodynamics and high-pressure melting curve from ab initio calculations. *Physical Review B*, *65*(16), 165118. https://doi.org/10.1103/PhysRevB.65.165118

Anderson, O. L. (2003). The three-dimensional phase diagram of iron. *Earth's core: Dynamics, structure, rotation*, *31*, 83–103. https://doi.org/10.1029/GD031p0083

Anzellini, S., Dewaele, A., Mezouar, M., Loubeyre, P., & Morard, G. (2013). Melting of iron at Earth's inner core boundary based on fast X-ray diffraction. *Science*, *340*(6131), 464–466. https://doi.org/10.1126/science.1233514

Bain, E. C. (1924). The nature of martensite. *Transactions of the American Institute of Mining and Metallurgical Engineers*, *70*, 25.

Belonoshko, A. B., Ahuja, R., & Johansson, B. (2003). Stability of the body-centred-cubic phase of iron in the Earth's inner core. *Nature*, *424*(6952), 1032–1034. https://doi.org/10.1038/nature01954

Belonoshko, A. B., Arapan, S., & Rosengren, A. (2011). An ab initio molecular dynamics study of iron phases at high pressure and temperature. *Journal of Physics: Condensed Matter*, *23*(48), 485402. https://doi.org/10.1088/0953-8984/23/48/485402

Belonoshko, A. B., Fu, J., Bryk, T., Simak, S. I., & Mattesini, M. (2019). Low viscosity of the Earth's inner core. *Nature communications*, *10*(1), 2483. https://doi.org/10.1038/s41467-019-10346-2

Belonoshko, A. B., Fu, J., & Smirnov, G. (2021). Free energies of iron phases at high pressure and temperature: Molecular dynamics study. *Physical Review B*, *104*(10), 104103. https://doi.org/10.1103/PhysRevB.104.104103

Belonoshko, A. B., Fu, J., & Smirnov, G. (2022). Erratum: Free energies of iron phases at high pressure and temperature: Molecular dynamics study. *Physical Review B*, *105*(5), 059903. https://doi.org/10.1103/PhysRevB.105.059903

Belonoshko, A. B., Lukinov, T., Fu, J., Zhao, J., Davis, S., & Simak, S. I. (2017). Stabilization of body-centred cubic iron under inner-core conditions. *Nature Geoscience*, *10*(4), 312–316. https://doi.org/10.1038/ngeo2892

Belonoshko, A. B., Simak, S. I., Olovsson, W., & Vekilova, O. Y. (2022). Elastic properties of body-centered cubic iron in Earth's inner core. *Physical Review B*, *105*(18), L180102. https://doi.org/10.1103/PhysRevB.105.L180102

Blöchl, P. E. (1994). Projector augmented-wave method. *Phys Rev B*, *50*(24), 17953–17979. https://doi.org/10.1103/PhysRevB.50.17953

Boehler, R. (1993). Temperatures in the Earth's core from melting-point measurements of iron at high static pressures. *Nature*, *363*(6429), 534–536. https://doi.org/10.1038/363534a0

Bouchet, J., Mazevet, S., Morard, G., Guyot, F., & Musella, R. (2013). Ab initio equation of state of iron up to 1500 GPa. *Physical Review B*, *87*(9), 094102.

https://doi.org/10.1103/PhysRevB.87.094102

Brown, J. M., & McQueen, R. G. (1986). Phase transitions, Grüneisen parameter, and elasticity for shocked iron between 77 GPa and 400 GPa. *Journal of Geophysical Research: Solid Earth*, *91*(B7), 7485–7494. https://doi.org/10.1029/JB091iB07p07485

Côté, A. S., Vočadlo, L., Dobson, D. P., Alfè, D., & Brodholt, J. P. (2010). Ab initio lattice dynamics calculations on the combined effect of temperature and silicon on the stability of different iron phases in the Earth's inner core. *Physics of the Earth and Planetary Interiors*, *178*(1-2), 2–7. https://doi.org/10.1016/j.pepi.2009.07.004

Cui, H., Zhang, Z., & Zhang, Y. (2013). The effect of Si and S on the stability of bcc iron with respect to tetragonal strain at the Earth's inner core conditions. *Geophysical Research Letters*, *40*(12), 2958–2962. https://doi.org/10.1002/grl.50582

Davies, C. J., Pozzo, M., & Alfè, D. (2019). Assessing the inner core nucleation paradox with atomic-scale simulations. *Earth and Planetary Science Letters*, *507*, 1–9. https://doi.org/10.1016/j.epsl.2018.11.019

Desjarlais, M. P. (2013). First-principles calculation of entropy for liquid metals. *Physical Review E*, *88*(6), 062145. https://doi.org/10.1103/PhysRevE.88.062145

Dewaele, A., Loubeyre, P., Occelli, F., Mezouar, M., Dorogokupets, P. I., & Torrent, M. (2006). Quasihydrostatic equation of state of iron above 2 Mbar. *Physical Review Letters*, *97*(21), 215504. https://doi.org/10.1103/PhysRevLett.97.215504

Dubrovinsky, L., Dubrovinskaia, N., Narygina, O., Kantor, I., Kuznetzov, A., Prakapenka, V., Vitos, L., Johansson, B., Mikhaylushkin, A., & Simak, S. (2007). Body-centered cubic iron-nickel alloy in Earth's core. *Science*, *316*(5833), 1880–1883. https://doi.org/10.1126/science.1142105

Dziewonski, A. M., & Anderson, D. L. (1981). Preliminary reference Earth model. *Physics of the Earth and Planetary Interiors*, *25*(4), 297–356. https://doi.org/10.17611/DP/9991844

Flyvbjerg, H., & Petersen, H. G. (1989). Error estimates on averages of correlated data. *The Journal of chemical physics*, *91*(1), 461–466. https://doi.org/10.1063/1.457480

Frenkel, D., & Smit, B. (2002). Understanding molecular simulation. *Academic Press, San Diego*. https://doi.org/10.1016/B978-0-12-267351-1.X5000-7

Gao, C., Ho, K.-M., Wentzcovitch, R. M., & Sun, Y. (2025). Understanding the two-step nucleation of iron at Earth's inner core conditions: A comparative molecular dynamics study. *Physical Review B*, *111*(13), 134104. https://doi.org/10.1103/PhysRevB.111.134104

Ghosh, M., Zhang, S., Hu, L., & Hu, S. X. (2023). Cooperative diffusion in body-centered cubic iron in Earth and super-Earths' inner core conditions. *Journal of Physics: Condensed Matter*, *35*(15), 154002. https://doi.org/10.1088/1361-648X/acba71

Gleason, A., & Mao, W. (2013). Strength of iron at core pressures and evidence for a weak Earth's inner core. *Nature Geoscience*, *6*(7), 571–574. https://doi.org/10.1038/ngeo1808

Godwal, B. K., González-Cataldo, F., Verma, A. K., Stixrude, L., & Jeanloz, R. (2015). Stability of iron crystal structures at 0.3–1.5 TPa. *Earth and Planetary Science Letters*, *409*, 299-306. https://doi.org/10.1016/j.epsl.2014.10.056

González-Cataldo, F., & Militzer, B. (2023). Ab initio determination of iron melting at

806 terapascal pressures and Super-Earths core crystallization. *Physical Review Research*,
807 5(3), 033194. https://doi.org/10.1103/PhysRevResearch.5.033194
808 Hernandez, J. A., Mohn, C. E., Guren, M. G., Baron, M. A., & Trønnes, R. G. (2022). Ab Initio
809 Atomistic Simulations of Ca-Perovskite Melting. *Geophysical Research Letters*,
810 *49*(20), e2021GL097262. https://doi.org/10.1029/2021GL097262
811 Hikosaka, K., Tagawa, S., Hirose, K., Okuda, Y., Oka, K., Umemoto, K., & Ohishi, Y. (2022).
812 Melting phase relations in Fe–Si–H at high pressure and implications for Earth's inner
813 core crystallization. *Scientific Reports*, *12*(1), 10000. https://doi.org/10.1038/s41598-
814 022-14106-z
815 Hirose, K., Wood, B., & Vočadlo, L. (2021). Light elements in the Earth's core. *Nature Reviews*
816 *Earth & Environment*, *2*(9), 645–658. https://doi.org/10.1038/s43017-021-00203-6
817 Hrubiak, R., Meng, Y., & Shen, G. (2018). Experimental evidence of a body centered cubic
818 iron at the Earth's core condition. *arXiv.*, 1804.05109.
819 https://doi.org/10.48550/arXiv.1804.05109
820 Ikuta, D., Ohtani, E., Fukui, H., Sakai, T., Ishikawa, D., & Baron, A. Q. (2022). Sound velocity
821 of hexagonal close-packed iron to the Earth's inner core pressure. *Nature*
822 *communications*, *13*(1), 7211. https://doi.org/10.1038/s41467-022-34789-2
823 Jana, R., & Caro, M. A. (2023). Searching for iron nanoparticles with a general-purpose
824 Gaussian approximation potential. *Physical Review B*, *107*(24), 245421.
825 https://doi.org/10.1103/PhysRevB.107.245421
826 Kohn, W., & Sham, L. J. (1965). Self-Consistent Equations Including Exchange and
827 Correlation Effects. *Physical Review*, *140*(4A), A1133–A1138.
828 https://doi.org/10.1103/physrev.140.a1133
829 Kraus, R. G., Hemley, R. J., Ali, S. J., Belof, J. L., Benedict, L. X., Bernier, J., Braun, D.,
830 Cohen, R., Collins, G. W., & Coppari, F. (2022). Measuring the melting curve of iron
831 at super-Earth core conditions. *Science*, *375*(6577), 202–205.
832 https://doi.org/10.1126/science.abm1472
833 Kresse, G., & Furthmüller, J. (1996). Efficient iterative schemes for ab initio total-energy
834 calculations using a plane-wave basis set. *Physical Review B*, *54*(16), 11169–11186.
835 https://doi.org/10.1103/physrevb.54.11169
836 Kuwayama, Y., Hirose, K., Sata, N., & Ohishi, Y. (2008). Phase relations of iron and iron–
837 nickel alloys up to 300 GPa: Implications for composition and structure of the Earth's
838 inner core. *Earth and Planetary Science Letters*, *273*(3-4), 379–385.
839 https://doi.org/10.1016/j.epsl.2008.07.001
840 Lai, P.-K., Hsieh, C.-M., & Lin, S.-T. (2012). Rapid determination of entropy and free energy
841 of mixtures from molecular dynamics simulations with the two-phase thermodynamic
842 model. *Physical Chemistry Chemical Physics*, *14*(43), 15206–15213.
843 https://doi.org/10.1039/C2CP42011B
844 Laio, A., Bernard, S., Chiarotti, G., Scandolo, S., & Tosatti, E. (2000). Physics of iron at Earth's
845 core conditions. *Science*, *287*(5455), 1027–1030.
846 https://doi.org/10.1126/science.287.5455.1027
847 Li, J., Wu, Q., Li, J., Xue, T., Tan, Y., Zhou, X., Zhang, Y., Xiong, Z., Gao, Z., & Sekine, T.
848 (2020). Shock melting curve of iron: A consensus on the temperature at the Earth's
849 inner core boundary. *Geophysical Research Letters*, *47*(15), e2020GL087758.

https://doi.org/10.1029/2020GL087758

Li, Y., Vočadlo, L., Brodholt, J., & Wood, I. (2016). Thermoelasticity of Fe_7C_3 under inner core conditions. *Journal of Geophysical Research: Solid Earth*, *121*(8), 5828–5837. https://doi.org/10.1002/2016JB013155

Li, Y., Vočadlo, L., & Brodholt, J. P. (2018). The elastic properties of hcp-Fe alloys under the conditions of the Earth's inner core. *Earth and Planetary Science Letters*, *493*, 118–127. https://doi.org/10.1016/j.epsl.2018.04.013

Li, Z., & Scandolo, S. (2022). Elasticity and Viscosity of hcp Iron at Earth's Inner Core Conditions From Machine Learning-Based Large-Scale Atomistic Simulations. *Geophysical Research Letters*, *49*(24), e2022GL101161. https://doi.org/10.1029/2022gl101161

Li, Z., & Scandolo, S. (2024a). Competing phases of iron at Earth's core conditions from deep-learning-aided ab-initio simulations. *Geophysical Research Letters*, *51*(19), e2024GL110357. https://doi.org/10.1029/2024GL110357

Li, Z., & Scandolo, S. (2024b). Deep-learning interatomic potential for iron at extreme conditions. *Physical Review B*, *109*(18), 184108. https://doi.org/10.1103/physrevb.109.184108

Lin, S.-T., Blanco, M., & Goddard III, W. A. (2003). The two-phase model for calculating thermodynamic properties of liquids from molecular dynamics: Validation for the phase diagram of Lennard-Jones fluids. *The Journal of Chemical Physics*, *119*(22), 11792–11805. https://doi.org/10.1063/1.1624057

Litasov, K. D., & Shatskiy, A. (2016). Composition of the Earth's core: A review. *Russian Geology and Geophysics*, *57*(1), 22–46. https://doi.org/10.1016/j.rgg.2016.01.003

Luo, W., Johansson, B., Eriksson, O., Arapan, S., Souvatzis, P., Katsnelson, M. I., & Ahuja, R. (2010). Dynamical stability of body center cubic iron at the Earth's core conditions. *Proceedings of the National Academy of Sciences*, *107*(22), 9962–9964. https://doi.org/10.1073/pnas.1004076107

Martorell, B., Brodholt, J., Wood, I. G., & Vočadlo, L. (2015). The elastic properties and stability of fcc-Fe and fcc-FeNi alloys at inner-core conditions. *Geophysical Journal International*, *202*(1), 94–101. https://doi.org/10.1093/gji/ggv128

Matsui, M., & Anderson, O. L. (1997). The case for a body-centered cubic phase (α′) for iron at inner core conditions. *Physics of the Earth and Planetary Interiors*, *103*(1-2), 55–62. https://doi.org/10.1016/S0031-9201(97)00020-4

Mattesini, M., Belonoshko, A. B., Buforn, E., Ramírez, M., Simak, S. I., Udias, A., Mao, H.-K., & Ahuja, R. (2010). Hemispherical anisotropic patterns of the Earth's inner core. *Proceedings of the National Academy of Sciences*, *107*(21), 9507–9512. https://doi.org/10.1073/pnas.1004856107

Mermin, N. D. (1965). Thermal properties of the inhomogeneous electron gas. *Physical Review*, *137*(5A), A1441–A1443. https://doi.org/10.1103/PhysRev.137.A1441

Mikhaylushkin, A. S., Simak, S. I., Dubrovinsky, L., Dubrovinskaia, N., Johansson, B., & Abrikosov, I. A. (2007). Pure iron compressed and heated to extreme conditions. *Physical Review Letters*, *99*(16), 165505. https://doi.org/10.1103/PhysRevLett.99.165505

Nosé, S. (1984). A unified formulation of the constant temperature molecular dynamics

894 methods. *The Journal of chemical physics*, *81*(1), 511–519.
895 https://doi.org/10.1063/1.447334
896 Ozolins, V. (2009). First-principles calculations of free energies of unstable phases: the case of
897 fcc W. *Physical Review Letters*, *102*(6), 065702.
898 https://doi.org/10.1103/PhysRevLett.102.065702
899 Perdew, J. P., Burke, K., & Ernzerhof, M. (1996). Generalized Gradient Approximation Made
900 Simple. *Physical Review Letters*, *77*(18), 3865–3868.
901 https://doi.org/10.1103/PhysRevLett.77.3865
902 Pushcharovsky, D. Y. (2019). Iron and its compounds in the Earth's core: New data and ideas.
903 *Geochemistry International*, *57*, 941–955.
904 https://doi.org/10.1134/S0016702919090088
905 Romanowicz, B., Cao, A., Godwal, B., Wenk, R., Ventosa, S., & Jeanloz, R. (2016). Seismic
906 anisotropy in the Earth's innermost inner core: Testing structural models against
907 mineral physics predictions. *Geophysical Research Letters*, *43*(1), 93–100.
908 https://doi.org/10.1002/2015GL066734
909 Ross, M., Young, D. A., & Grover, R. (1990). Theory of the iron phase diagram at Earth core
910 conditions. *Journal of Geophysical Research: Solid Earth*, *95*(B13), 21713-21716.
911 https://doi.org/10.1029/JB095iB13p21713
912 Schultz, A. J., Moustafa, S. G., & Kofke, D. A. (2018). No system-size anomalies in entropy
913 of bcc iron at Earth's inner-core conditions. *Scientific Reports*, *8*(1), 7295.
914 https://doi.org/10.1038/s41598-018-25419-3
915 Sha, X., & Cohen, R. (2010). Elastic isotropy of ε-Fe under Earth's core conditions.
916 *Geophysical Research Letters*, *37*(10), L10302.
917 https://doi.org/10.1029/2009GL042224
918 Shen, G., Mao, H. k., Hemley, R. J., Duffy, T. S., & Rivers, M. L. (1998). Melting and crystal
919 structure of iron at high pressures and temperatures. *Geophysical Research Letters*,
920 *25*(3), 373–376. https://doi.org/10.1029/97GL03776
921 Sinmyo, R., Hirose, K., & Ohishi, Y. (2019). Melting curve of iron to 290 GPa determined in
922 a resistance-heated diamond-anvil cell. *Earth and Planetary Science Letters*, *510*, 45–
923 52. https://doi.org/10.1016/J.EPSL.2019.01.006
924 Soderlind, P., Moriarty, J. A., & Wills, J. M. (1996). First-principles theory of iron up to earth-
925 core pressures: Structural, vibrational, and elastic properties. *Physical Review B:*
926 *Condens Matter*, *53*(21), 14063–14072. https://doi.org/10.1103/physrevb.53.14063
927 Sola, E., & Alfe, D. (2009). Melting of Iron under Earth's Core Conditions from Diffusion
928 Monte Carlo Free Energy Calculations. *Physical Review Letters*, *103*(7), 078501.
929 https://doi.org/10.1103/PhysRevLett.103.078501
930 Steinle-Neumann, G., Stixrude, L., Cohen, R., & Gülseren, O. (2001). Elasticity of iron at the
931 temperature of the Earth's inner core. *Nature*, *413*(6851), 57–60.
932 https://doi.org/10.1038/35092536
933 Stixrude, L. (2012). Structure of iron to 1 Gbar and 40, 000 K. *Physical Review Letters*, *108*(5),
934 055505. https://doi.org/10.1103/PhysRevLett.108.055505
935 Stixrude, L., & Cohen, R. E. (1995). Constraintson the crystallinestructure of the inner core:
936 Mechanical instability of BCC iron at high pressure. *Geophysical Research Letters*,
937 *22*(2), 125–128. https://doi.org/10.1029/94GL02742

938 Sun, T., Brodholt, J. P., Li, Y., & Vočadlo, L. (2018). Melting properties from ab initio free
939 energy calculations: Iron at the Earth's inner-core boundary. *Physical Review B*, *98*(22),
940 224301. https://doi.org/10.1103/PhysRevB.98.224301
941 Sun, T., Xian, J., Zhang, H., Zhang, Z., & Zhang, Y. (2017). Two-phase thermodynamic model
942 for computing entropies of liquids reanalyzed. *The Journal of Chemical Physics*,
943 *147*(19), 194505. https://doi.org/10.1063/1.5001798
944 Sun, Y., Mendelev, M. I., Zhang, F., Liu, X., Da, B., Wang, C.-Z., Wentzcovitch, R. M., & Ho,
945 K.-M. (2024). Unveiling the effect of Ni on the formation and structure of Earth's inner
946 core. *Proceedings of the National Academy of Sciences*, 121(4), e2316477121.
947 https://doi.org/10.1073/pnas.2316477121
948 Sun, Y., Mendelev, M. I., Zhang, F., Liu, X., Da, B., Wang, C. Z., Wentzcovitch, R. M., & Ho,
949 K. M. (2023). Ab Initio Melting Temperatures of Bcc and Hcp Iron Under the Earth's
950 Inner Core Condition. *Geophysical Research Letters*, *50*(5), e2022GL102447.
951 https://doi.org/10.1029/2022gl102447
952 Sun, Y., Zhang, F., Mendelev, M. I., Wentzcovitch, R. M., & Ho, K. M. (2022). Two-step
953 nucleation of the Earth's inner core. *Proceedings of the National Academy of Sciences*,
954 *119*(2), e2113059119. https://doi.org/10.1073/pnas.2113059119
955 Tateno, S., Hirose, K., Ohishi, Y., & Tatsumi, Y. (2010). The structure of iron in Earth's inner
956 core. *Science*, *330*, 359–361. https://doi.org/10.1126/science.1194662
957 Tateno, S., Ozawa, H., Hirose, K., Suzuki, T., I-Kawaguchi, S., & Hirao, N. (2019). Fe_2S: The
958 Most Fe-Rich Iron Sulfide at the Earth's Inner Core Pressures. *Geophysical Research*
959 *Letters*, *46*(21), 11944–11949. https://doi.org/10.1029/2019GL085248
960 Turneaure, S. J., Sharma, S. M., & Gupta, Y. M. (2020). Crystal Structure and Melting of Fe
961 Shock Compressed to 273 GPa: In Situ X-Ray Diffraction. *Physical Review Letters*,
962 *125*(21), 215702. https://doi.org/10.1103/PhysRevLett.125.215702
963 Vočadlo, L., Alfè, D., Gillan, M. J., Wood, I. G., Brodholt, J. P., & Price, G. D. (2003). Possible
964 thermal and chemical stabilization of body-centred-cubic iron in the Earth's core.
965 *Nature*, *424*(6948), 532–536. https://doi.org/10.1038/nature01829
966 Vočadlo, L., Brodholt, J., Alfè, D., Gillan, M. J., & Price, G. D. (2000). Ab initio free energy
967 calculations on the polymorphs of iron at core conditions. *Physics of the Earth and*
968 *Planetary Interiors*, *117*(1-4), 123–137. https://doi.org/10.1016/S0031-
969 9201(99)00092-8
970 Vočadlo, L., Brodholt, J., Alfè, D., Price, G. D., & Gillan, M. J. (1999). The structure of iron
971 under the conditions of the Earth's inner core. *Geophysical Research Letters*, *26*(9),
972 1231–1234. https://doi.org/10.1029/1999GL900214
973 Vočadlo, L., Wood, I. G., Alfè, D., & Price, G. D. (2008). Ab initio calculations on the free
974 energy and high P–T elasticity of face-centred-cubic iron. *Earth and Planetary Science*
975 *Letters*, *268*(3-4), 444–449. https://doi.org/10.1016/j.epsl.2008.01.043
976 Vočadlo, L., Wood, I. G., Gillan, M. J., Brodholt, J., Dobson, D. P., Price, G. D., & Alfè, D.
977 (2008). The stability of bcc-Fe at high pressures and temperatures with respect to
978 tetragonal strain. *Physics of the Earth and Planetary Interiors*, *170*(1-2), 52–59.
979 https://doi.org/10.1016/j.pepi.2008.07.032
980 Williams, Q., Jeanloz, R., Bass, J., Svendsen, B., & Ahrens, T. J. (1987). The melting curve of
981 iron to 250 gigapascals: A constraint on the temperature at Earth's center. *Science*,

236(4798), 181–182. https://doi.org/10.1126/science.236.4798.181

Wilson, A., & Stixrude, L. (2021). Entropy, dynamics, and freezing of $CaSiO_3$ liquid. *Geochimica et Cosmochimica Acta*, *302*, 1–17. https://doi.org/10.1016/j.gca.2021.03.015

Wilson, A. J., Alfè, D., Walker, A. M., & Davies, C. J. (2023). Can homogeneous nucleation resolve the inner core nucleation paradox? *Earth and Planetary Science Letters*, *614*, 118176. https://doi.org/10.1016/j.epsl.2023.118176

Wu, F., Wu, S., Wang, C.-Z., Ho, K.-M., Wentzcovitch, R. M., & Sun, Y. (2024). Melting temperature of iron under the Earth's inner core condition from deep machine learning. *Geoscience Frontiers*, *15*(6), 101925. https://doi.org/10.1016/j.gsf.2024.101925

Xu, Y., He, Y., Sun, S., Zhang, W., Dai, W., Kim, D. Y., & Li, H. (2025). Viscosities of hcp iron alloys under Earth's inner core conditions. *Geoscience Frontiers*, *16*(1), 101935. https://doi.org/10.1016/j.gsf.2024.101935

Yang, H., Dou, P., Xiao, T., Li, Y., Muir, J. M. R., & Zhang, F. (2023). The Geophysical Properties of FeH_x Phases Under Inner Core Conditions. *Geophysical Research Letters*, *50*(22), e2023GL104493. https://doi.org/10.1029/2023gl104493

Yang, H., Wan, L., Li, Y., Vočadlo, L., & Brodholt, J. (2025). Molecular-Dynamics Study of the Crystal Structure of Iron Under the Earth's Inner Core Conditions (Version 1). *Figshare*. [Dataset]. https://figshare.com/s/18ba3094bc4496753b5d

Yuan, L., & Steinle-Neumann, G. (2023). Hydrogen distribution between the Earth's inner and outer core. *Earth and Planetary Science Letters*, *609*, 118084. https://doi.org/10.1016/j.epsl.2023.118084

Zhang, S., Panjwani, A., Xiao, P., Ghosh, M., Ogitsu, T., Ping, Y., & Hu, S. (2025). Thermally induced structural competitiveness and metastability of body-centered-cubic iron under nonequilibrium conditions. *Physical Review B*, *111*(22), 224106. https://doi.org/10.1103/ws64-kmzr

Zhang, Y., Wang, Y., Huang, Y., Wang, J., Liang, Z., Hao, L., Gao, Z., Li, J., Wu, Q., & Zhang, H. (2023). Collective motion in hcp-Fe at Earth's inner core conditions. *Proceedings of the National Academy of Sciences*, *120*(41), e2309952120. https://doi.org/10.1073/pnas.2309952120

Zhang, Z., Csányi, G., & Alfè, D. (2020). Partitioning of sulfur between solid and liquid iron under Earth's core conditions: Constraints from atomistic simulations with machine learning potentials. *Geochimica et Cosmochimica Acta*, *291*, 5–18. https://doi.org/10.1016/j.gca.2020.03.028

Zwanzig, R. W. (1954). High-temperature equation of state by a perturbation method. I. Nonpolar gases. *The Journal of Chemical Physics*, *22*(8), 1420–1426. https://doi.org/10.1063/1.1740409

References From the Supporting Information

Jana, R., & Caro, M. A. (2023). Searching for iron nanoparticles with a general-purpose Gaussian approximation potential. *Physical Review B*, 107(24), 245421. https://doi.org/10.1103/PhysRevB.107.245421